applied sciences

MDPI

Article

Three-Dimensional Acoustic Analysis of a Rectangular Duct with Gradient Cross-Sections in High-Speed Trains: A Theoretical Derivation

Yanhong Sun, Yi Qiu, Lianyun Liu * and Xu Zheng *

College of Energy Engineering, Zhejiang University, Hangzhou 310027, China; sunyanhong@zju.edu.cn (Y.S.); yiqiu@zju.edu.cn (Y.Q.)
* Correspondence: lianyun.liu@zju.edu.cn (L.L.); zhengxu@zju.edu.cn (X.Z.)

Featured Application: The purpose of this work was to provide a detailed derivation process of the 3D analytical solution and TMs of the RDGCs based on the previous studies on the variable ducts and propose a certain reference for designing and improving the acoustic characteristics of the duct systems used in high-speed trains.

Abstract: Rectangular ducts used in the air-conditioning system of a high-speed train should be carefully designed to achieve optimal acoustic and flow performance. However, the theoretical analysis of the rectangular ducts with gradient cross-sections (RDGC) at frequencies higher than the one-dimensional cut-off frequency is rarely published. This paper has developed the three-dimensional analytical solutions to the wave equations of the expanding and shrinking RDGCs. Firstly, a homogeneous second-order variable coefficient differential equation is derived from the wave equations. Two coefficients of the solution to the differential equation are set to zero to ensure convergence. Secondly, the transfer matrices of the duct systems composed of multiple RDGCs are derived from the three-dimensional solutions. The transmission losses of the duct systems are then calculated from the transfer matrices and validated with the measurement. Finally, the acoustic performance and flow efficiency of the RDGCs with different geometries are discussed. The results show that the REC with double baffles distributed transversely has good performance in both acoustic attenuation and flow efficiency. This study shall provide a helpful guide for designing rectangular ducts used in high-speed trains.

Keywords: theoretical derivation; three-dimensional wave equation; rectangular duct with gradient cross-sections; transfer matrix

Citation: Sun, Y.; Qiu, Y.; Liu, L.; Zheng, X. Three-Dimensional Acoustic Analysis of a Rectangular Duct with Gradient Cross-Sections in High-Speed Trains: A Theoretical Derivation. *Appl. Sci.* **2022**, *12*, 5307. https://doi.org/10.3390/app12115307

Academic Editor: Suchao Xie

Received: 3 May 2022
Accepted: 23 May 2022
Published: 24 May 2022

1. Introduction

Rectangular ducts are used in the air-conditioning systems of high-speed trains+ to guide airflow. Some rectangular ducts adopt the oblique baffles (Figure 1) to form the varying cross-sections which improve the performance of the ducts in noise attenuation [1].

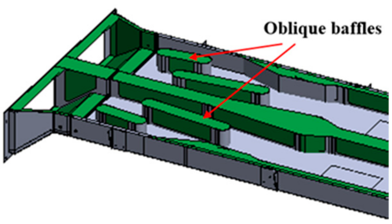

Figure 1. Rectangular ducts used in a Fuxing bullet train.

The current studies on the duct acoustics of high-speed train are practiced based on simulation, such as the hybrid method of finite element and statistical energy analysis

(FE-SEA) [1,2]. Most scholars have focused their research on ducts suitable for any vehicle based on a variety of methods. Both analytical and numerical methods have been widely used in the field of duct acoustics. Generally, the numerical methods, such as the finite element method (FEM) [3–6], boundary element method (BEM) [7] and computational fluid dynamics (CFD) method [8–10], are popular for analyzing duct systems with complex geometries. Assis et al. [4] proposed a spectral FEM approach to compute the transfer matrix (TM) of duct systems with arbitrary geometries. Liu et al. [8] proposed the time domain CFD approaches to predict the acoustic performance of the duct systems without and with mean flow.

On the other hand, the analytical method is more efficient in computation than the numerical methods. Two types of analytical methods have been used to investigate a duct system with varying cross–sections. The Wentzel–Kramers–Brillouin (WKB) method [11–15] utilizes the high frequency approximation that allows to neglect certain terms in the nonlinear governing equations of the media in a duct. Subrahmanyam et al. [12] used the WKB approximation to derive the exact solutions for one-dimensional (1D) ducts with area variations in the absence of mean flow. Rani et al. [14,15] derived a WKB-type solution to the generalized Helmholtz equation in 1D ducts with nonuniform cross-sectional areas and inhomogeneity in mean flow. The WKB approximation is less accurate than solving the full wave equations of the duct. The solutions to the wave equations of 1D ducts with varying cross-sections have been studied for decades [16–23]. Pillai et al. [24] developed the 1D solution to a horn-like rectangular duct at frequencies lower than 250 Hz. However, the three-dimensional (3D) solutions to the wave equations in rectangular ducts with gradient cross-sections (RDGCs), which are more accurate at higher frequencies than the 1D solutions, are rarely seen.

The objective of this paper is to develop the 3D analytical solutions to the wave equations of the expanding or shrinking RDGCs at frequencies up to 1600 Hz. The derived solutions are used to obtain the TMs and transmission losses (TLs) of the duct systems consisted of RDGCs, which have been validated with the measured results. Lastly, the effects of the RDGC geometries on the acoustic performance and flow efficiency of the duct systems are discussed.

The organization of this paper is as follows: Section 2 develops the 3D analytical solutions to the wave equations of RDGCs. In Section 3, the TMs of the RDGCs are derived. In Section 4, several duct systems consisting of RDGCs are modeled to obtain the TMs. The TLs and pressure losses of the duct systems with different RDGC geometries are obtained and discussed in Section 5. Finally, the conclusions are presented in Section 6.

2. 3D Analytical Solutions to the Wave Equations of a RDGC

2.1. 3D Solutions for a Straight Rectangular Duct

Figure 2 shows a uniform rectangular duct with a width of b and a height of h. The 3D wave equation of the rectangular duct is given by [25]

$$\frac{\partial^2 p}{\partial t^2} = c^2 \nabla^2 p, \tag{1}$$

where p, t and c are the sound pressure, advancing time and sound velocity, respectively. The Laplacian operator ∇^2 is given as follows:

$$\nabla^2 = \frac{\partial^2}{\partial x^2} + \frac{\partial^2}{\partial y^2} + \frac{\partial^2}{\partial z^2} \tag{2}$$

where x, y and z are the Cartesian coordinates shown in Figure 2.

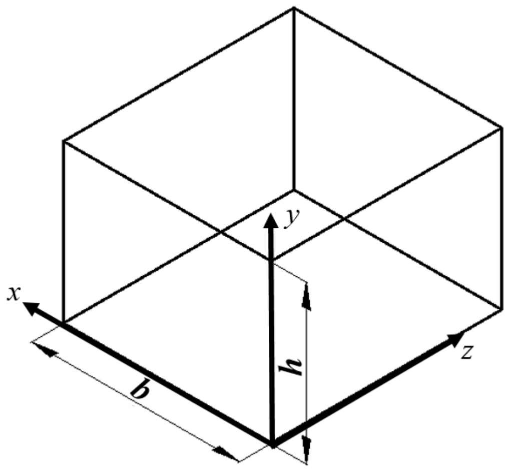

Figure 2. A straight rectangular duct.

The general solution of Equation (1) [25] is

$$p(x,y,z,t) = \left(C_1 e^{-\mathrm{j}k_z z} + C_2 e^{+\mathrm{j}k_z z}\right)\left(e^{-\mathrm{j}k_x x} + C_3 e^{+\mathrm{j}k_x x}\right)\left(e^{-\mathrm{j}k_y y} + C_4 e^{+\mathrm{j}k_y y}\right)e^{\mathrm{j}\omega t} \quad (3)$$

where j is the imaginary unit. C_1, C_2, C_3 and C_4 are the coefficients to be determined with boundary conditions. k_x and k_y are the wave numbers in the x and y direction, respectively. k_z is defined as

$$k_z = \sqrt{k^2 - {k_x}^2 - {k_y}^2} \quad (4)$$

where $k = \omega/c$ and ω is the angular frequency. The solution of the rigid-walled duct with a width of b and a height of h is given by

$$p(x,y,z,t) = \sum_{m=0}^{\infty}\sum_{n=0}^{\infty}\cos\left(\frac{m\pi x}{b}\right)\cos\left(\frac{n\pi y}{h}\right)p(z,t) \quad (5)$$

where $p(z,t) = \left(C_{1,mn}e^{-\mathrm{j}k_{z,mn}z} + C_{2,mn}e^{+\mathrm{j}k_{z,mn}z}\right)e^{\mathrm{j}\omega t}$ and $k_{z,mn} = \sqrt{k^2 - (m\pi/b)^2 - (n\pi/h)^2}$. Here, $\cos(m\pi x/b)\cos(n\pi y/h)$ is an eigenfunction representing the wave shape in the x-y plane at the (m, n) mode. $C_{1,mn}$ and $C_{2,mn}$ are the amplitudes of the waves at the (m, n) mode propagating in the positive and negative z directions.

2.2. 3D Solutions for a RDGC

A RDGC with either expanding (positive θ) or shrinking (negative θ) sections is shown in Figure 3. θ is the angle between the bevel edge and the z axis. b_i and b_o are the widths of the inlet and the outlet, respectively.

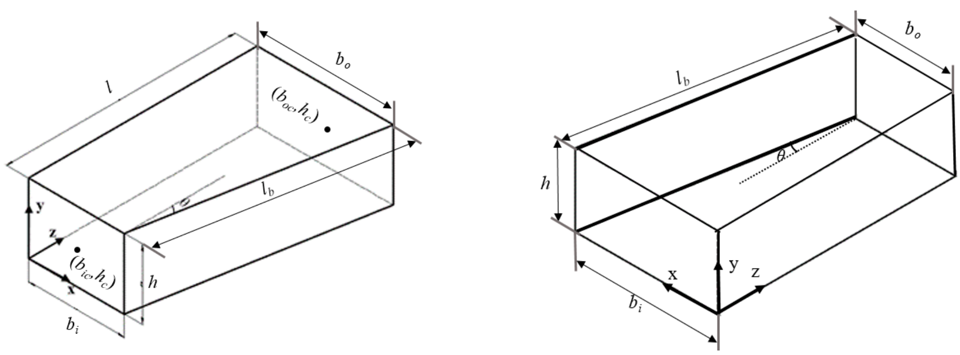

(a) (b)

Figure 3. (**a**) A rectangular duct with expanding sections, (**b**) a rectangular duct with shrinking sections.

Since the cross-sectional area S changes along the z direction, the 1D sound wave equation in the z direction is obtained with modifying Equation (1) as

$$\frac{1}{S}\frac{\partial}{\partial z}\left(S\frac{\partial p}{\partial z}\right) = \frac{1}{c^2}\frac{\partial^2 p}{\partial t^2}. \tag{6}$$

For an expanding duct, S is given by

$$S = (z\tan\theta + b_i)h \tag{7}$$

Substituting Equation (7) into Equation (6) yields a homogeneous second-order variable coefficient differential equation as follows:

$$\frac{\partial^2 p}{\partial z^2} + \frac{\tan\theta}{z\tan\theta + b_i}\frac{\partial p}{\partial z} = \frac{1}{c^2}\frac{\partial^2 p}{\partial t^2}. \tag{8}$$

The solution of Equation (8) is given by [26]

$$p(z,t) = \{B_+ \mathrm{J}_0(k_z\alpha) + B_- \mathrm{J}_0(-k_z\alpha) + C_+ \mathrm{K}_0(-\mathrm{j}k_z\alpha) + C_- \mathrm{K}_0(\mathrm{j}k_z\alpha)\}e^{\mathrm{j}\omega t} \tag{9}$$

where $\alpha = z + b_i/\tan\theta$. The quantities B_+, B_-, C_+ and C_- are the corresponding amplitudes. $\mathrm{J}_0(.)$ is the zeroth order of the Bessel function of the first kind, and $\mathrm{K}_0(.)$ is the zeroth order of the modified Bessel function of the second kind [27]. When $k_z\alpha$ becomes imaginary, the values of $\mathrm{J}_0(k_z\alpha)$ and $\mathrm{J}_0(-k_z\alpha)$ are possible to be infinite. To converge the solution, B_+ and B_- are set to zero. As a result, Equation (9) is simplified as

$$p(z,t) = \{C_+ \mathrm{K}_0(-\mathrm{j}k_z\alpha) + C_- \mathrm{K}_0(\mathrm{j}k_z\alpha)\}e^{\mathrm{j}\omega t}. \tag{10}$$

Substituting Equation (10) into Equation (5), with b replaced by $b_i + z\tan\theta$, the 3D solution of an expanding RDGC is derived as

$$p(x,y,z,t) = \sum_{m=0}^{\infty}\sum_{n=0}^{\infty}\cos\left(\frac{m\pi x}{\alpha\tan\theta}\right)\cos\left(\frac{n\pi y}{h}\right)\{C_{+,mn}\mathrm{K}_0(-\mathrm{j}k_{z,mn}\alpha) + C_{-,mn}\mathrm{K}_0(\mathrm{j}k_{z,mn}\alpha)\}e^{\mathrm{j}\omega t} \tag{11}$$

$$k_{z,mn} = \sqrt{k^2 - \left(\frac{m\pi}{\alpha\tan\theta}\right)^2 - (n\pi/h)^2} \tag{12}$$

where $C_{+,mn}$ and $C_{-,mn}$ are the coefficients to be determined with boundary conditions.

Solve the momentum equation [25]

$$\frac{\partial v}{\partial t} = -\frac{1}{\rho_0}\nabla\cdot p \tag{13}$$

to give the particle velocity v of an expanding RDGC as follows:

$$\begin{aligned} v(x,y,z,t) = &-\tfrac{1}{\rho_0\omega}\sum_{m=0}^{\infty}\sum_{n=0}^{\infty} k_{z,mn}\cos\left(\tfrac{m\pi x}{\alpha\tan\theta}\right)\cos\left(\tfrac{n\pi y}{h}\right)\{C_{+,mn}\mathrm{K}_1(-\mathrm{j}k_{z,mn}\alpha) - C_{-,mn}\mathrm{K}_1(\mathrm{j}k_{z,mn}\alpha)\}e^{\mathrm{j}\omega t} \\ &\underbrace{+\left(-\frac{1}{j\rho_0\omega}\right)\sum_{m=0}^{\infty}\sum_{n=0}^{\infty}\frac{m\pi x}{\alpha^2\tan\theta}\sin\left(\frac{m\pi x}{\alpha\tan\theta}\right)\cos\left(\frac{n\pi y}{h}\right)\{C_{+,mn}\mathrm{K}_0(-\mathrm{j}k_{z,mn}\alpha) + C_{-,mn}\mathrm{K}_0(\mathrm{j}k_{z,mn}\alpha)\}e^{\mathrm{j}\omega t}}_{X} \end{aligned} \tag{14}$$

where ρ_0 is the ambient air density and $\mathrm{K}_1(.)$ is the first order of the modified Bessel function of the second kind.

The derivation of the solutions for a shrinking RDGC is similar to that of an expanding RDGC and gives the same equations of Equations (11) and (14) with a negative θ.

3. Derivation of the TM for a RDGC

The transfer matrix $\mathbf{T}$ ($\begin{bmatrix} A & B \\ C & D \end{bmatrix}$) is used to describe the relationship as follows:

$$\begin{bmatrix} p_i \\ v_i \end{bmatrix} = \begin{bmatrix} A & B \\ C & D \end{bmatrix} \begin{bmatrix} p_o \\ v_o \end{bmatrix} \tag{15}$$

where v_i and v_o are the average particle velocities at the inlet and outlet of a duct system. The quantities p_i and p_o are the inlet and outlet average sound pressures defined with

$$p_i = \frac{1}{S_i} \iint_{S_i} p(x, y, 0) \mathrm{d}x\mathrm{d}y \tag{16}$$

$$p_o = \frac{1}{S_o} \iint_{S_o} p(x, y, l) \mathrm{d}x\mathrm{d}y \tag{17}$$

where l is the length of the duct. The quantities S_i and S_o are the inlet and outlet cross-sectional areas, respectively. The four elements of the TM can be obtained as follows:

$$\begin{cases} A = (p_i/p_o)|_{v_o=0} \\ C = (v_i/p_o)|_{v_o=0} \end{cases} \tag{18}$$

$$\begin{cases} B = \{(p_i - Ap_o)/v_o\}|_{v_i=0} \\ D = (-Cp_o/v_o)|_{v_i=0} \end{cases}. \tag{19}$$

The elements A, B, C and D can be calculated from Appendix A.

The transfer matrix $\mathbf{T'}$ ($\begin{bmatrix} A' & B' \\ C' & D' \end{bmatrix}$) of the shrinking RDGC is derived from the $\mathbf{T}$ with a negative θ.

4. The TMs and TLs of Rectangular Expansion Chambers (RECs)

4.1. The TMs of the RECs with One or Double Baffles

To simplify the setup of a validation experiment, the circular ducts with a diameter of 50 mm are added at the inlet and outlet of the rectangular chamber with a height (h) of 150 mm. The dimensions of the REC with one baffle are shown in Figure 4. The dimensional parameters of REC are designed according to those of the branch rectangular ducts in high-speed trains. The center **o** of the baffle coincides with that of the REC. All the RECs in the following sections have the same circular ducts and rectangular chamber as those in Figure 4.

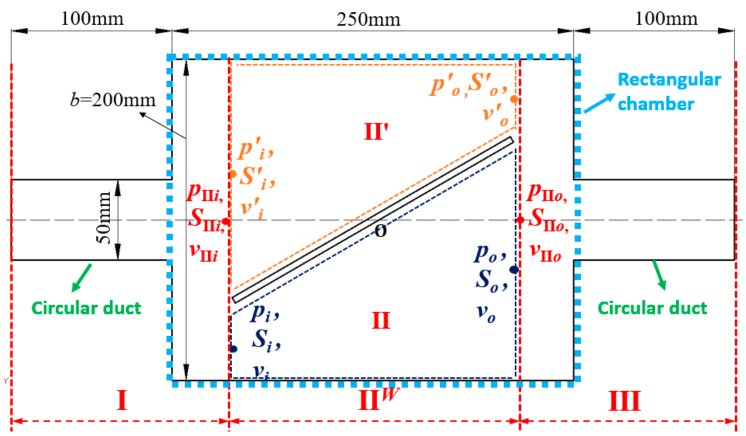

Figure 4. The gemometry of the REC with one baffle.

The components of the REC with one baffle are specified in Table 1.

Table 1. Description of each component of the REC with one baffle.

Unit	TM	Annotations
I	$\mathbf{T}_{\mathrm{I}}$	—made of two uniform ducts and one sudden expansion section
II^W	$\mathbf{T}_{\mathrm{II}}^W$	—made of an expanding RDGC (II) and a shrinking RDGC (II′)
III	$\mathbf{T}_{\mathrm{III}}$	—made of two uniform ducts and one sudden contraction section

The transfer matrices ($\mathbf{T}_{\mathrm{II}}$ and $\mathbf{T}_{\mathrm{II}}'$) of the expanding RDGC and the shrinking RDGC are given by

$$\mathbf{T}_{\mathrm{II}} = \begin{bmatrix} A_{\mathrm{II}} & B_{\mathrm{II}} \\ C_{\mathrm{II}} & D_{\mathrm{II}} \end{bmatrix}, \mathbf{T}'_{\mathrm{II}} = \begin{bmatrix} A'_{\mathrm{II}} & B'_{\mathrm{II}} \\ C'_{\mathrm{II}} & D'_{\mathrm{II}} \end{bmatrix}. \tag{20}$$

According to the notation in Figure 4, the state variables at the two ends of each RDGC are related by

$$\begin{bmatrix} p_i \\ v_i \end{bmatrix} = \mathbf{T}_{\mathrm{II}} \begin{bmatrix} p_o \\ v_o \end{bmatrix}, \begin{bmatrix} p'_i \\ v'_i \end{bmatrix} = \mathbf{T}'_{\mathrm{II}} \begin{bmatrix} p'_o \\ v'_o \end{bmatrix}. \tag{21}$$

The continuity of pressure and mass velocity at the inlet and outlet of the component II^W gives

$$p_{\mathrm{II}\,i} = p_i = p'_i, p_{\mathrm{II}\,o} = p_o = p'_o \tag{22}$$

$$S_{\mathrm{II}\,i} v_{\mathrm{II}\,i} = S_i v_i + S'_i v'_i, S_{\mathrm{II}\,o} v_{\mathrm{II}\,o} = S_o v_o + S'_o v'_o \tag{23}$$

where $'$ denote the variables of the shrinking RDGC. $S_{\mathrm{II}\,i}$ and $S_{\mathrm{II}\,o}$ represent the cross-sectional areas at the inlet and outlet of the component II^W, respectively. Solving simultaneously Equations (21)–(23) yields [28]

$$\begin{bmatrix} p_{\mathrm{II}\,i} \\ v_{\mathrm{II}\,i} \end{bmatrix} = \mathbf{T}_{\mathrm{II}}^W \begin{bmatrix} p_{\mathrm{II}\,o} \\ v_{\mathrm{II}\,o} \end{bmatrix} = \begin{bmatrix} A_{\mathrm{II}}^W & B_{\mathrm{II}}^W \\ C_{\mathrm{II}}^W & D_{\mathrm{II}}^W \end{bmatrix} \begin{bmatrix} p_{\mathrm{II}\,o} \\ v_{\mathrm{II}\,o} \end{bmatrix}. \tag{24}$$

The terms of the TM are given by

$$\begin{cases} A_{\mathrm{II}}^W = \frac{A'_{\mathrm{II}} B_{\mathrm{II}} S_o + A_{\mathrm{II}} B'_{\mathrm{II}} S'_o}{B_{\mathrm{II}} S_o + B'_{\mathrm{II}} S'_o} \\ B_{\mathrm{II}}^W = \frac{B_{\mathrm{II}} B'_{\mathrm{II}} S_{\mathrm{II}\,o}}{B_{\mathrm{II}} S_o + B'_{\mathrm{II}} S'_o} \\ C_{\mathrm{II}}^W = \frac{\left(D_{\mathrm{II}} S_o S'_i - D'_{\mathrm{II}} S'_o S_i\right)\left(A'_{\mathrm{II}} - A_{\mathrm{II}}\right)}{\left(B_{\mathrm{II}} S_o + B'_{\mathrm{II}} S'_o\right) S_{\mathrm{II}\,i}} + \frac{S'_i C_{\mathrm{II}} + S_i C'_{\mathrm{II}}}{S_{\mathrm{II}\,i}} \\ D_{\mathrm{II}}^W = \frac{\left(D_{\mathrm{II}} S_o S'_i - D'_{\mathrm{II}} S'_o S_i\right) B'_{\mathrm{II}} S_{\mathrm{II}\,o}}{\left(B_{\mathrm{II}} S_o + B'_{\mathrm{II}} S'_o\right) S'_o S_{\mathrm{II}\,i}} + \frac{S_{\mathrm{II}\,o} S_i D'_{\mathrm{II}}}{S_o S_{\mathrm{II}\,i}} \end{cases} \tag{25}$$

The TM of the REC with one baffle is calculated with

$$\mathbf{T}_1 = \mathbf{T}_I \mathbf{T}_{\mathrm{II}}^W \mathbf{T}_{\mathrm{III}} = \begin{bmatrix} T_{11} & T_{12} \\ T_{21} & T_{22} \end{bmatrix}. \tag{26}$$

where $\mathbf{T}_I$ and $\mathbf{T}_{\mathrm{III}}$ are calculated with the analytical solutions in the refs. [29,30].

The cut-off frequencies at the mode (m, n) of a duct with a rectangular section can be calculated with

$$f_{cut-off} = \frac{c}{2}\sqrt{\left(\frac{m}{b}\right)^2 + \left(\frac{n}{h}\right)^2}. \tag{27}$$

Table 2 shows the calculated cut-off frequencies with $m, n \leq 2$ of the rectangular chamber (Figure 4). The maximum cut-off frequency at (2, 2) mode is 2858.3 Hz. As a result, the number of modes with $m, n \leq 2$ is enough to investigate the acoustic characteristics of the RECs at frequencies below 1600 Hz.

Table 2. Modal frequencies (Hz) of the rectangular chamber.

n \ *m*	0	1	2
0	0	857.5	1715.0
1	1143.3	1429.2	2061.2
2	2286.7	2442.2	2858.3

Figures 5 and 6 show the geometries of the RECs with double baffles distributed either axially or transversely. The distance between the centers (o_1 and o_2) of the baffles is 100 mm. The $\mathbf{T}_I$ and $\mathbf{T}_{\mathrm{III}}$ in Figures 5 and 6 are exactly the same as those in Figure 4. $\mathbf{T}_{\mathrm{II}}^W$ and $\mathbf{T}_V^W$ in Figure 5 are calculated with the Equation (25), while the $\mathbf{T}_{\mathrm{IV}}$ of the straight rectangular duct is obtained with the analytical solutions in the ref. [29].

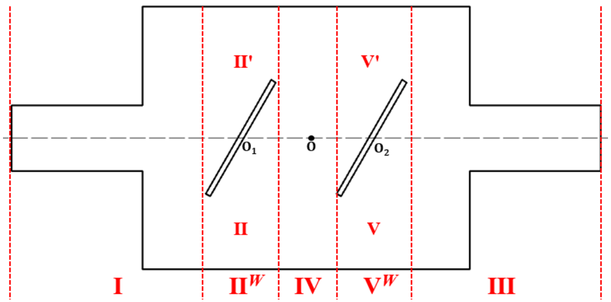

Figure 5. The REC with double baffles distributed axially.

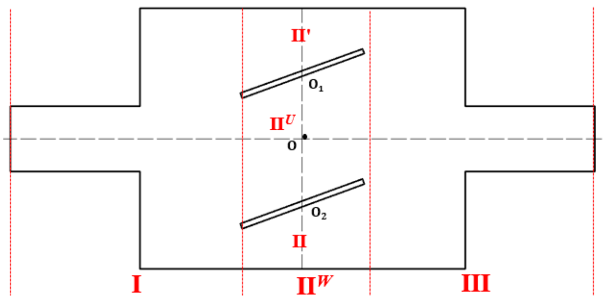

Figure 6. The REC with double baffles distributed transversely.

The transfer matrices ($\mathbf{T}_{\mathrm{II}}$, $\mathbf{T}_{\mathrm{II}}{}'$ and $\mathbf{T}_{\mathrm{II}}^U$) of the expanding RDGC, the shrinking RDGC and the uniform duct (II^U) in Figure 6 are given by

$$\mathbf{T}_{\mathrm{II}} = \begin{bmatrix} A_{\mathrm{II}} & B_{\mathrm{II}} \\ C_{\mathrm{II}} & D_{\mathrm{II}} \end{bmatrix}, \mathbf{T}_{\mathrm{II}}' = \begin{bmatrix} A_{\mathrm{II}}' & B_{\mathrm{II}}' \\ C_{\mathrm{II}}' & D_{\mathrm{II}}' \end{bmatrix}, \mathbf{T}_{\mathrm{II}}^U = \begin{bmatrix} A_{\mathrm{II}}^U & B_{\mathrm{II}}^U \\ C_{\mathrm{II}}^U & D_{\mathrm{II}}^U \end{bmatrix}. \tag{28}$$

The transfer matrix ($\mathbf{T}_{\mathrm{II}}^W$) of the component II^W is calculated with a similar process presented in the Equations (21)–(24) and the four elements are given by

$$\begin{cases} A_{\mathrm{II}}^W & = \frac{A_{\mathrm{II}}^U B_{\mathrm{II}}' B_{\mathrm{II}} S_o^U + A_{\mathrm{II}}' B_{\mathrm{II}}^U B_{\mathrm{II}} S_i^U + A_{\mathrm{II}} B_{\mathrm{II}}' B_{\mathrm{II}}^U S_o}{B_{\mathrm{II}}' B_{\mathrm{II}} S_o^U + B_{\mathrm{II}}^U B_{\mathrm{II}} S_o' + B_{\mathrm{II}}' B_{\mathrm{II}}^U S_o} \\ B_{\mathrm{II}}^W & = \frac{B_{\mathrm{II}}' B_{\mathrm{II}}^U B_{\mathrm{II}} S_{\mathrm{II}\,o}}{B_{\mathrm{II}}' B_{\mathrm{II}} S_o^U + B_{\mathrm{II}}^U B_{\mathrm{II}} S_o' + B_{\mathrm{II}}' B_{\mathrm{II}}^U S_o} \\ C_{\mathrm{II}}^W & = \frac{A_{\mathrm{II}}^U B_{\mathrm{II}}' B_{\mathrm{II}} S_o^U + A_{\mathrm{II}}' B_{\mathrm{II}}^U B_{\mathrm{II}} S_o' + A_{\mathrm{II}} B_{\mathrm{II}}' B_{\mathrm{II}}^U S_o}{B_{\mathrm{II}}' B_{\mathrm{II}} S_o^U + B_{\mathrm{II}}^U B_{\mathrm{II}} S_o' + B_{\mathrm{II}}' B_{\mathrm{II}}^U S_o} \left(\frac{D_{\mathrm{II}}' S_i'}{B_{\mathrm{II}}' S_{\mathrm{II}\,i}} + \frac{D_{\mathrm{II}}^U S_i^U}{B_{\mathrm{II}}^U S_{\mathrm{II}\,i}} + \frac{D_{\mathrm{II}} S_i}{B_{\mathrm{II}} S_{\mathrm{II}\,i}} \right) \\ & - \left(\frac{A_{\mathrm{II}}' D_{\mathrm{II}}' S_i'}{B_{\mathrm{II}}' S_{\mathrm{II}\,i}} + \frac{A_{\mathrm{II}}^U D_{\mathrm{II}}^U S_i^U}{B_{\mathrm{II}}^U S_{\mathrm{II}\,i}} + \frac{A_{\mathrm{II}} D_{\mathrm{II}} S_i}{B_{\mathrm{II}} S_{\mathrm{II}\,i}} \right) + \frac{S_i' C_{\mathrm{II}}' + S_i^U C_{\mathrm{II}}^U + S_i C_{\mathrm{II}}}{S_{\mathrm{II}\,i}} \\ D_{\mathrm{II}}^W & = \frac{S_{\mathrm{II}\,o} (D_{\mathrm{II}}' B_{\mathrm{II}}^U B_{\mathrm{II}} S_i' + D_{\mathrm{II}}^U B_{\mathrm{II}}' B_{\mathrm{II}} S_i^U + D_{\mathrm{II}} B_{\mathrm{II}}' B_{\mathrm{II}}^U S_i)}{S_{\mathrm{II}\,i} (B_{\mathrm{II}}' B_{\mathrm{II}} S_o^U + B_{\mathrm{II}}^U B_{\mathrm{II}} S_o' + B_{\mathrm{II}}' B_{\mathrm{II}}^U S_o)} \end{cases} \tag{29}$$

where S_i^U and S_o^U are the cross-sectional areas of the inlet and outlet of the component II^U. The TM ($\mathbf{T}_{2a}$) of the REC with double baffles distributed axially and the TM ($\mathbf{T}_{2t}$) with double baffles distributed transversely are given by

$$\mathbf{T}_{2a} = \mathbf{T}_I \mathbf{T}_{\mathrm{II}}^W \mathbf{T}_{\mathrm{IV}} \mathbf{T}_V^W \mathbf{T}_{\mathrm{III}} \tag{30}$$

$$\mathbf{T}_{2t} = \mathbf{T}_I \mathbf{T}_{\mathrm{II}}^W \mathbf{T}_{\mathrm{III}}. \tag{31}$$

4.2. Geometries of the RECs

Table 3 shows the geometries of the RECs with different baffle configurations. All the baffles in the RECs have a thickness of 4 mm.

Table 3. The geometries of the RECs with different baffle configurations.

Type 1	Case 1-0	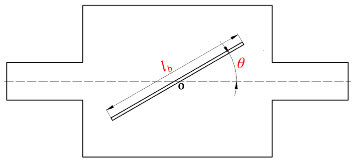	$l_b = 0.50b$, $\theta = 40°$
	Case 1-1		$l_b = 0.50b$, $\theta = 20°$
	Case 1-2		$l_b = 0.50b$, $\theta = 60°$
	Case 1-3		$l_b = 0.30b$, $\theta = 40°$
	Case 1-4	The REC with one baffle	$l_b = 0.40b$, $\theta = 40°$
Type 2a	Case 2a-0	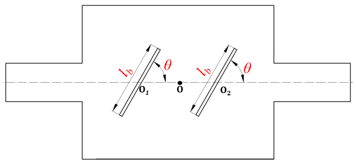	$l_b = 0.50b$, $\theta = 40°$
	Case 2a-1		$l_b = 0.50b$, $\theta = 20°$
	Case 2a-2		$l_b = 0.50b$, $\theta = 60°$
	Case 2a-3		$l_b = 0.30b$, $\theta = 40°$
	Case 2a-4	The REC with double baffles distributed axially	$l_b = 0.40b$, $\theta = 40°$
Type 2t	Case 2t-0	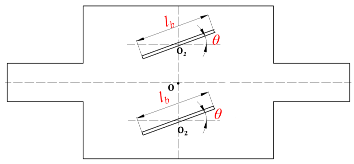	$l_b = 0.50b$, $\theta = 40°$
	Case 2t-1		$l_b = 0.50b$, $\theta = 20°$
	Case 2t-2		$l_b = 0.50b$, $\theta = 60°$
	Case 2t-3		$l_b = 0.30b$, $\theta = 40°$
	Case 2t-4	The REC with double baffles distributed transversely	$l_b = 0.40b$, $\theta = 40°$

4.3. Calculation and Measurement of the TLs for the RECs

The TL of a REC can be calculated from the derived TM as follows:

$$\mathrm{TL} = 20\log_{10}\left(\frac{1}{2}\left|T_{11} + \frac{T_{12}}{\rho_0 c} + T_{21}\cdot\rho_0 c + T_{22}\right|\right). \tag{32}$$

To verify the accuracy of the analytical method, the TLs of the RECs (Case 1-1, Case 2a-1 and Case 2t-1) were measured with the two-load method [31] shown in Figure 7. The sound source was located at the outside of a semi-anechoic room where a REC with baffles was located. An acoustic stimulus was introduced into the REC through a metal duct, where two microphones were placed with a distance of 40 mm. The other two microphones were located with the same distance at the duct connected to the outlet of the REC. A Brüel & Kjær (B&K) 3560 C Module was adopted to acquire the data sampled with a frequency of 16,384 Hz. The experimental parameters are given in Table 4.

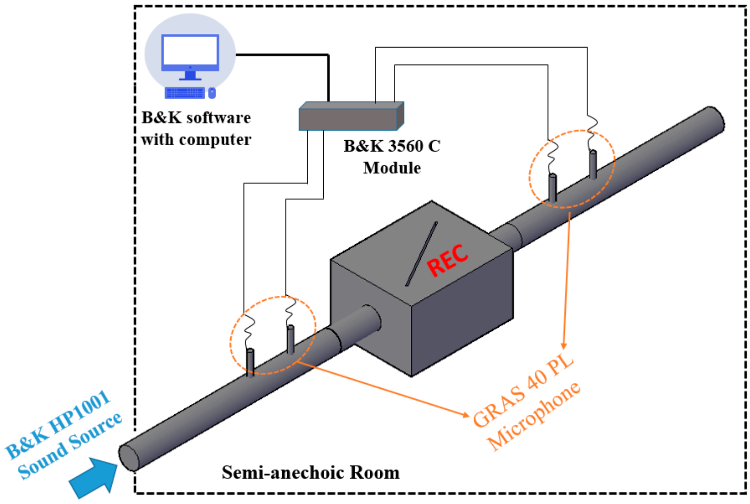

Figure 7. Experimental setup for measuring the TL of a REC.

Table 4. Experimental parameters.

Parameters	Values
Temperature	24.5 °C
Relative humidity	29.2%
Pressure	101,300 Pa

5. Results

5.1. Experimental Validation of the Calculated Results

In order to verify the 3D analytical method, the TLs obtained by experiment, 3D analytical method and FEM are shown in Figure 8. The FEM model and boundary conditions are shown in Appendix B. Generally, the calculated results are in good agreement with the measured results and the accuracy of the analytical method is validated to a certain degree. However, the frequencies of TL peaks from FEM agree less with the experimental results than those obtained by the 3D analytical method in this paper. The inaccuracy of the measured TLs below 200 Hz shown in the Case 1-1 of Figure 8 should be attributed to the insufficient energy of the sound source in this frequency range. As a result, the TLs below 200 Hz are not presented in the other cases of Figure 8. The discrepancies between the experiment and the 3D analytical method at higher frequencies may be caused by the following reasons. First, the analytical method regards the REC as rigid, while the prototypes under test are made of plastic with certain elasticity. Second, the damping in the air is ignored with the analytical method. Third, the ignorance of the $B_{+}J_0(k_z\alpha)$, $B_{-}J_0(-k_z\alpha)$ in the Equation (9) and the X in Equation (14) also causes errors.

5.2. TLs of the RECs

The TLs of the RECs with one or double baffles are shown in Figures 9 and 10. It can be seen that the peaks and troughs of the TL curves of all types move to a lower frequency with the decreasing θ and increasing l_b. Although the Type 2a has more TL peaks, it is worse in performance than the Type 2t at frequencies from 500 Hz to 1100 Hz. Generally, the Type 2t is better in acoustic performance than the other types, especially at frequencies from 600 Hz to 1100 Hz.

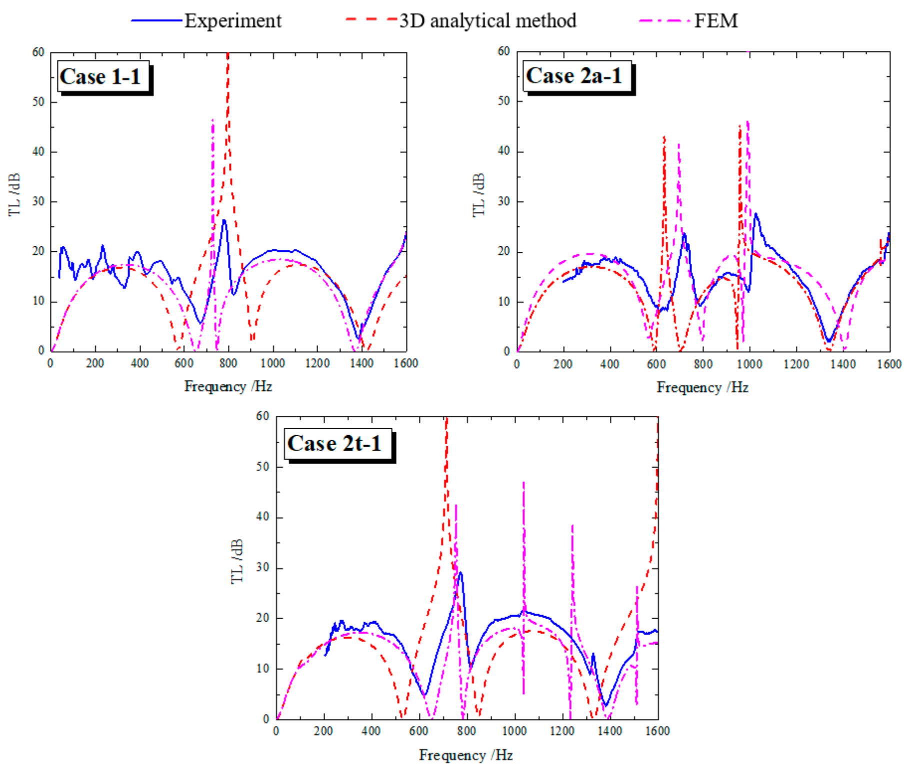

Figure 8. The comparison of TLs obtained by experiment, 3D analytical method and FEM.

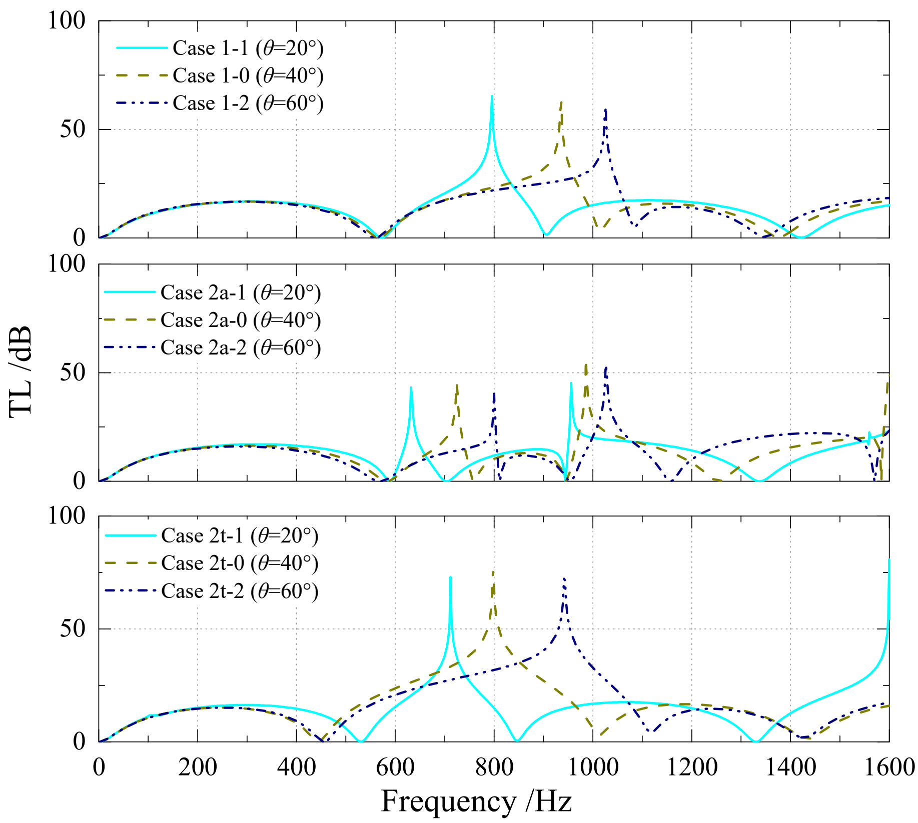

Figure 9. TLs of the RECs with different baffle angles.

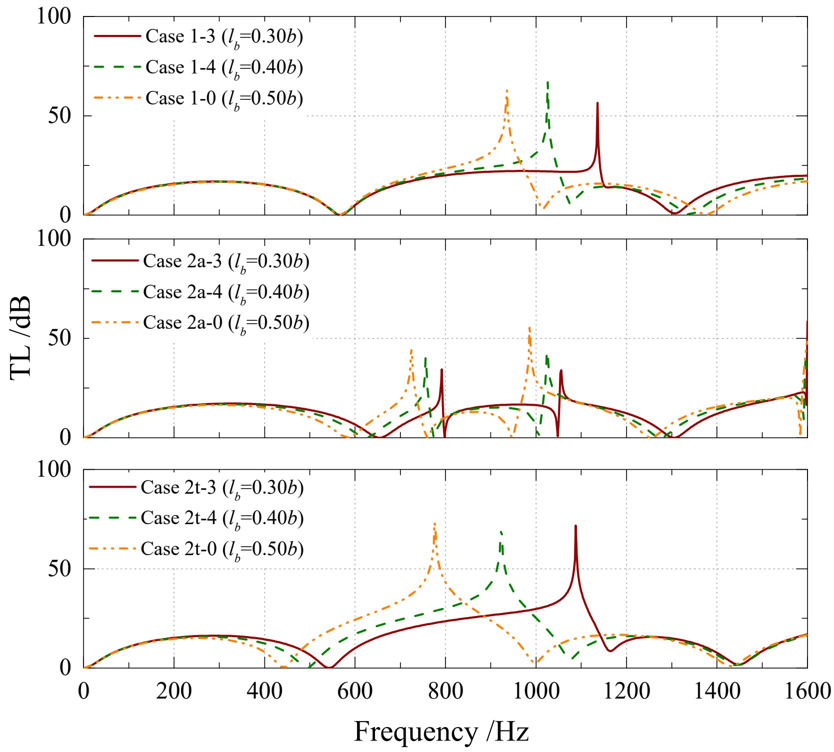

Figure 10. TLs of the RECs with different baffle lengths.

5.3. Pressure Losses of the RECs

The improvement of the acoustic performance of a duct system cannot be at the expense of flow efficiency. A CFD model [32] (Figure 11), using the standard k-ε turbulence model, is adopted to calculate the difference (pressure loss) between the area-weighted average pressures at the inlet and outlet of the RECs. The model is discretized by about one million unstructured tetrahedral meshes with a mesh size of 3 mm. The inlet has a velocity of 10 m/s and the outlet has a zero gauge pressure.

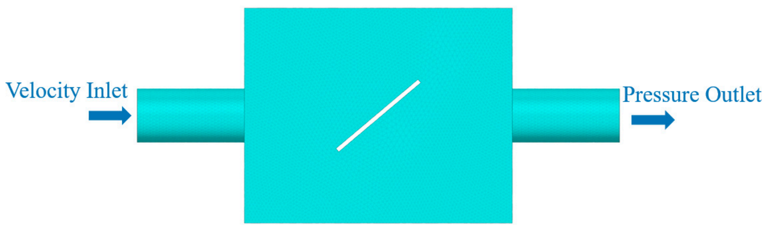

Figure 11. CFD model of the REC with one baffle.

Table 5 shows the pressure losses of the RECs with one baffle or double baffles. It can be seen that the pressure losses of the Case 1-0 and Case 2a-0 are higher than the Case 2t-0. Therefore, the REC with double baffles distributed transversely (Type 2t) has good performance in both flow efficiency and TL.

Table 5. The pressure losses of the RECs with different baffle configurations.

Case 1-0	Case 2a-0	Case 2t-0
141 Pa	140.2 Pa	117.7 Pa

The influence of the baffle angles and lengths on the pressure losses of the RECs are shown in Figures 12 and 13. Figure 12 shows that the pressure losses of Type 1 and Type 2t increase as θ increases, while the pressure loss of Type 2a decreases as θ increases from 40° to 60°. Figure 13 shows that Type 1 and Type 2a have much higher pressure losses than Type 2t, while the pressure loss of Type 2t increases faster than Type 1 and Type 2a as l_b increases. In general, Type 2t has better performance in flow efficiency than the other types, especially at small values of θ and l_b.

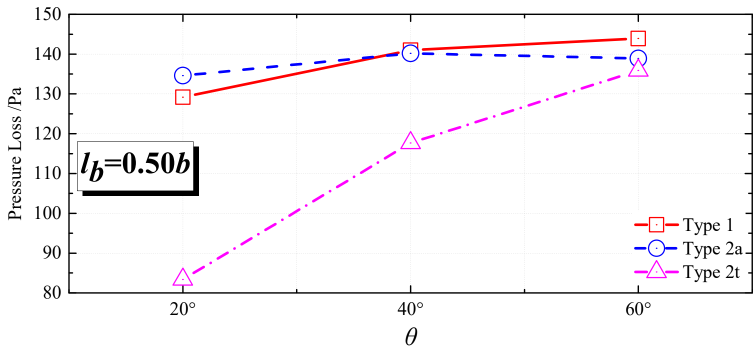

Figure 12. The pressure losses of the RECs with different baffle angles.

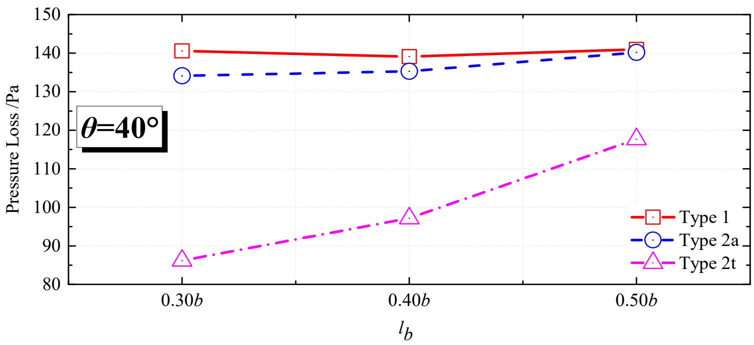

Figure 13. The pressure losses of the RECs with different baffle lengths.

6. Conclusions

Here, the 3D analytical solutions to the wave equations of the expanding and shrinking RDGCs were derived. The TMs of the RECs consisted of multiple expanding and shrinking RDGCs, which were then calculated from the 3D solutions. The TLs calculated from the TMs were validated with the measured results.

In the derivation of the 3D analytical solution and TMs of the RDGC, the ignorance of some infinite and complex terms is risky, but it can simplify the formulas and reduce the computation. These behaviors are proved to be practicable by experiments and the TLs obtained by the theories in this paper are accurate to a certain extent.

According to the TLs of the RECs with different baffle configurations, the peaks and troughs of the TL curves of all types move to a higher frequency with the increasing angle (θ) between the bevel edge and the axial direction and move to a lower frequency with the increasing length (l_b) of the baffle. The REC with double baffles distributed transversely (Type 2t) is better in acoustic performance than the other types at frequencies from 600 Hz to 1100 Hz. On the other hand, although the pressure losses of all types of RECs increase as θ or l_b increases, Type 2t always has a lower pressure loss than types. In summary, Type 2t generally has good performance in both acoustic attenuation and flow efficiency.

This achievement of research shall provide a certain reference for designing and improving the acoustic characteristics of the duct systems used in high-speed trains.

Author Contributions: This article was prepared through the collective efforts of all the authors. Conceptualization, methodology, and writing—original draft preparation, Y.S.; validation, Y.S. and L.L.; writing—review and editing, Y.Q. and X.Z. All authors have read and agreed to the published version of the manuscript.

Funding: This research was supported by the National Natural Science Foundation of China (Grant No. 51975515 and No. 51905474).

Institutional Review Board Statement: The study did not involve humans or animals.

Informed Consent Statement: The study did not involve humans.

Data Availability Statement: The data that support the findings of this study are available from the corresponding author upon reasonable request.

Conflicts of Interest: The authors declared no potential conflict of interest with respect to the research, authorship and/or publication of this article.

Appendix A. Derivation of the *A*, *B*, *C* and *D* in the TM

We set $v(x,y,0)$ and $v(x,y,l)$ as $\overline{v}$ and 0, respectivley, where $\overline{v}$ is the harmonic excitation with a constant amplitude. As a result, v_i and v_o are also equal to $\overline{v}$ and 0. To simplify the expression, $\mathrm{j}k_{z,mn}\alpha$ is denoted as β_{mn}. Substituting $v(x,y,0)=\overline{v}$ into Equation (14) and eliminating the $e^{\mathrm{j}\omega t}$ yields

$$-\frac{1}{\rho_0\omega}\sum_{m=0}^{\infty}\sum_{n=0}^{\infty}k_{z,mn,i}\cos\left(\frac{m\pi x}{b_i}\right)\cos\left(\frac{n\pi y}{h}\right)\{C_{+,mn}\mathrm{K}_1(-\beta_{i,mn})-C_{-,mn}\mathrm{K}_1(\beta_{i,mn})\}=\overline{v}. \tag{A1}$$

The X term in Equation (14) is ignored here, because it is too complicated to derive a concise solution. The rationality of this mathematical operation has been verified by the following experimental results.

Substituting $v(x,y,l)=0$ into Equation (14) and ignoring the term X yields

$$C_{+,mn}\mathrm{K}_1(-\beta_{o,mn})-C_{-,mn}\mathrm{K}_1(\beta_{o,mn})=0. \tag{A2}$$

The quantities $\beta_{i,mn}$ and $\beta_{o,mn}$ represent the β_{mn} at z = 0 and z = l, respectively. $k_{z,mn,i}$ and $k_{z,mn,o}$ represent the $k_{z,mn}$ at z = 0 and z = l, respectively.

In order to obtain the coefficients $C_{+,mn}$ and $C_{-,mn}$, operating the both sides of Equation (A1) with $\iint_{S_i}\cos(m'\pi x/b_i)\cos(n'\pi y/h)\mathrm{d}x\mathrm{d}y$ [28] yields

$$\begin{aligned}&\iint_{S_i}\overline{v}\cos\left(\frac{m'\pi x}{b_i}\right)\cos\left(\frac{n'\pi y}{h}\right)\mathrm{d}x\mathrm{d}y\\&=-\frac{1}{\rho_0\omega}\sum_{m,m'=0}^{\infty}\sum_{n,n'=0}^{\infty}k_{z,mn,i}\iint_{S_i}\cos(\frac{m'\pi x}{b_i})\cos(\frac{n'\pi y}{h})\cos(\frac{m\pi x}{b_i})\cos(\frac{n\pi y}{h})\mathrm{d}x\mathrm{d}y\{C_{+,mn}\mathrm{K}_1(-\beta_{i,mn})-C_{-,mn}\mathrm{K}_1(\beta_{i,mn})\}.\end{aligned} \tag{A3}$$

According to the orthogonality property of eigenfunctions, Equation (A3) is transformed with $m=m'$ and $n=n'$ to the following equation:

$$\iint_{S_i}\overline{v}\cos\left(\frac{m\pi x}{b_i}\right)\cos\left(\frac{n\pi y}{h}\right)\mathrm{d}x\mathrm{d}y=-\frac{1}{\rho_0\omega}k_{z,mn,i}\iint_{S_i}\cos^2(\frac{m\pi x}{b_i})\cos^2(\frac{n\pi y}{h})\mathrm{d}x\mathrm{d}y\{C_{+,mn}\mathrm{K}_1(-\beta_{i,mn})-C_{-,mn}\mathrm{K}_1(\beta_{i,mn})\}. \tag{A4}$$

The coefficients $C_{+,mn}$ and $C_{-,mn}$ can be calculated from Equations (A2) and (A4) as follows:

$$C_{+,mn}=-\rho_0c\overline{v}\frac{k\mathrm{K}_1(\beta_{o,mn})}{k_{z,mn,i}W(k_{z,mn})}\frac{\iint_{S_i}\cos(\frac{m\pi x}{b_i})\cos(\frac{n\pi y}{h})\mathrm{d}x\mathrm{d}y}{\iint_{S_i}\cos^2(\frac{m\pi x}{b_i})\cos^2(\frac{n\pi y}{h})\mathrm{d}x\mathrm{d}y} \tag{A5}$$

$$C_{-,mn}=\frac{C_{+,mn}\mathrm{K}_1(-\beta_{o,mn})}{\mathrm{K}_1(\beta_{o,mn})} \tag{A6}$$

where

$$W(k_{z,mn})=\mathrm{K}_1(-\beta_{i,mn})\mathrm{K}_1(\beta_{o,mn})-\mathrm{K}_1(\beta_{i,mn})\mathrm{K}_1(-\beta_{o,mn}). \tag{A7}$$

Substituting Equations (A5) and (A6) into Equation (11), the 3D solution of the pressure is obtained as follows:

$$p(x,y,z)=-\rho_0c\overline{v}\sum_{m=0}^{\infty}\sum_{n=0}^{\infty}\frac{V(k_{z,mn},z)}{W(k_{z,mn})}\frac{k}{k_{z,mn,i}}\frac{\cos(\frac{m\pi x}{b_i+z\tan\theta})\cos(\frac{n\pi y}{h})\iint_{S_i}\cos(\frac{m\pi x}{b_i})\cos(\frac{n\pi y}{h})\mathrm{d}x\mathrm{d}y}{\iint_{S_i}\cos^2(\frac{m\pi x}{b_i})\cos^2(\frac{n\pi y}{h})\mathrm{d}x\mathrm{d}y} \tag{A8}$$

where

$$V(k_{z,mn}, z) = \mathrm{K}_1(\beta_{o,mn})\mathrm{K}_0(-\beta_{mn}) + \mathrm{K}_0(\beta_{mn})\mathrm{K}_1(-\beta_{o,mn}). \tag{A9}$$

Substituting Equation (A8) with z = 0 into Equation (16) to obtain the average pressure at the inlet as follows:

$$\begin{aligned}
p_i &= \frac{1}{S_i}\iint_{S_i}\left\{-\rho_0 c\overline{v}\sum_{m=0}^{\infty}\sum_{n=0}^{\infty}\frac{V(k_{z,mn},0)}{W(k_{z,mn})}\frac{k}{k_{z,mn,i}}\frac{\cos(\frac{m\pi x}{b_i})\cos(\frac{n\pi y}{h})\iint_{S_i}\cos(\frac{m\pi x}{b_i})\cos(\frac{n\pi y}{h})\mathrm{d}x\mathrm{d}y}{\iint_{S_i}\cos^2(\frac{m\pi x}{b_i})\cos^2(\frac{n\pi y}{h})\mathrm{d}x\mathrm{d}y}\right\}\mathrm{d}x\mathrm{d}y \\
&= -\rho_0 c\overline{v}_1\left\{\begin{array}{l}
\underbrace{\frac{V(k,0)}{W(k)}}_{E_{11}} + \underbrace{\sum_{m=1}^{\infty}\frac{V(k_{z,m0,i},0)}{W(k_{z,m0})}\frac{2k}{k_{z,m0,i}}\left(\frac{2}{m\pi}\Psi_{b1}\right)^2}_{E_{12}} \\
\quad + \underbrace{\sum_{n=1}^{\infty}\frac{V(k_{z,0n,i},0)}{W(k_{z,0n})}\frac{2k}{k_{z,0n,i}}\left(\frac{2}{n\pi}\Psi_{h1}\right)^2}_{E_{13}} \\
\quad + \underbrace{\sum_{m=1}^{\infty}\sum_{n=1}^{\infty}\frac{V(k_{z,mn,i},0)}{W(k_{z,mn})}\frac{4k}{k_{z,mn,i}}\left(\frac{4}{mn\pi^2}\Psi_{b1}\Psi_{h1}\right)^2}_{E_{14}}
\end{array}\right\} \\
&= -\rho_0 c\overline{v}_1 E_1
\end{aligned} \tag{A10}$$

where

$$E_1 = E_{11} + E_{12} + E_{13} + E_{14} \tag{A11}$$

$$\Psi_{b1} = \cos\left(\frac{m\pi b_{ic}}{b_i}\right)\sin\left(\frac{m\pi}{2}\right) \tag{A12}$$

$$\Psi_{h1} = \cos\left(\frac{n\pi h_c}{h}\right)\sin\left(\frac{n\pi}{2}\right). \tag{A13}$$

The quantity E_{11} is obtained with $m = 0$ and $n = 0$. E_{12} is obtained with $m \geq 1$ and $n = 0$. E_{13} is obtained with $m = 0$ and $n \geq 1$. Additionally, E_{14} is obtained with $m \geq 1$ and $n \geq 1$. (b_{ic}, h_c) are the coordinates of the center point at the inlet shown in Figure 3.

Substituting Equation (A8) with z = l into Equation (17) to obtain the average pressure at the outlet as follows:

$$\begin{aligned}
p_o &= \frac{1}{S_o}\iint_{S_o}\left\{-\rho_0 c\overline{v}_1\sum_{m=0}^{\infty}\sum_{n=0}^{\infty}\frac{V(k_{z,mn},l)}{W(k_{z,mn})}\frac{k}{k_{z,mn,i}}\frac{\cos(\frac{m\pi x}{b_i+l\tan\theta})\cos(\frac{n\pi y}{h})\iint_{S_i}\cos(\frac{m\pi x}{b_i})\cos(\frac{n\pi y}{h})\mathrm{d}x\mathrm{d}y}{\iint_{S_i}\cos^2(\frac{m\pi x}{b_i})\cos^2(\frac{n\pi y}{h})\mathrm{d}x\mathrm{d}y}\right\}\mathrm{d}x\mathrm{d}y \\
&= -\rho_0 c\overline{v}\left\{\begin{array}{l}
\underbrace{\frac{V(k,l)}{W(k)}}_{E_{21}} + \underbrace{\sum_{m=1}^{\infty}\frac{V(k_{z,m0,o},l)}{W(k_{z,m0})}\frac{2k}{k_{z,m0,i}}\left(\frac{2}{m\pi}\right)^2\Psi_{lb2}\Psi_{b1}}_{E_{22}} \\
\quad + \underbrace{\sum_{n=1}^{\infty}\frac{V(k_{z,0n,o},l)}{W(k_{z,0n})}\frac{2k}{k_{z,0n,i}}\left(\frac{2}{n\pi}\right)^2\Psi_{h1}\Psi_{h2}}_{E_{23}} \\
\quad + \underbrace{\sum_{m=1}^{\infty}\sum_{n=1}^{\infty}\frac{V(k_{z,mn,o},l)}{W(k_{z,mn})}\frac{4k}{k_{z,mn,i}}\left(\frac{4}{mn\pi^2}\right)^2\Psi_{b1}\Psi_{h1}\Psi_{lb2}\Psi_{h2}}_{E_{24}}
\end{array}\right\} \\
&= -\rho_0 c\overline{v}E_2
\end{aligned} \tag{A14}$$

where

$$E_2 = E_{21} + E_{22} + E_{23} + E_{24} \tag{A15}$$

$$\Psi_{h2} = \cos\left(\frac{n\pi h_c}{h}\right)\sin\left(\frac{n\pi}{2}\right) \tag{A16}$$

$$\Psi_{lb2} = \cos\left(\frac{m\pi b_{oc}}{b_o}\right)\sin\left(\frac{m\pi}{2}\right). \tag{A17}$$

The quantity E_{21} is obtained with $m = 0$ and $n = 0$. E_{22} is obtained with $m \geq 1$ and $n = 0$. E_{23} is obtained with $m = 0$ and $n \geq 1$. Additionally, E_{24} is obtained with $m \geq 1$ and $n \geq 1$. (b_{oc}, h_c) are the coordinates of the center point at the outlet in Figure 3.

The elements A and C can be calculated from Equations (18), (A10) and (A14) with the following equations

$$A = \frac{-\rho_0 c \overline{v} E_1}{-\rho_0 c \overline{v} E_2} = \frac{E_1}{E_2} \tag{A18}$$

$$C = \frac{v_i}{-\rho_0 c \overline{v}_1 E_{12}} = \frac{\overline{v}}{-\rho_0 c \overline{v} E_2} = \frac{-1}{\rho_0 c E_2}. \tag{A19}$$

We set $v(x, y, 0)$ and $v(x, y, l)$ as 0 and $\overline{v}$, respectively, and obtain $v_i = 0$ and $v_o = \overline{v}$. Substituting $v(x, y, 0) = 0$ into Equation (14) yields

$$C_{+,mn} \mathrm{K}_1(-\beta_{i,mn}) - C_{-,mn} \mathrm{K}_1(\beta_{i,mn}) = 0. \tag{A20}$$

Substituting $v(x, y, l) = \overline{v}$ into Equation (14) yields

$$-\frac{1}{\rho_0 \omega} \sum_{m=0}^{\infty} \sum_{n=0}^{\infty} k_{z,mn,o} \cos\left(\frac{m\pi x}{b_i + l\tan\theta}\right) \cos\left(\frac{n\pi y}{h}\right) \{C_{+,mn} \mathrm{K}_1(-\beta_{o,mn}) - C_{-,mn} \mathrm{K}_1(\beta_{o,mn})\} = \overline{v}. \tag{A21}$$

Operating the both sides of Equation (A21) with $\iint_{S_o} \cos\{m\pi x/(b_i + l\tan\theta)\} \cos(n\pi y/h)$ $\mathrm{d}x\mathrm{d}y$ and using the same transformation with $m = m'$ and $n = n'$ as in Equation (A3) yields

$$\begin{aligned} &\iint_{S_o} \overline{v} \cos\left(\tfrac{m\pi x}{b_i + l\tan\theta}\right) \cos\left(\tfrac{n\pi y}{h}\right) \mathrm{d}x\mathrm{d}y \\ &= -\tfrac{1}{\rho_0 \omega} k_{z,mn,o} \iint_{S_o} \cos^2\left(\tfrac{m\pi x}{b_i + l\tan\theta}\right) \cos^2\left(\tfrac{n\pi y}{h}\right) \mathrm{d}x\mathrm{d}y \{C_{+,mn} \mathrm{K}_1(-\beta_{o,mn}) - C_{-,mn} \mathrm{K}_1(\beta_{o,mn})\}. \end{aligned} \tag{A22}$$

The coefficients $C_{+,mn}$ and $C_{-,mn}$ can be obtained from Equations (A20) and (A22) as follows:

$$C_{+,mn} = \rho_0 c \overline{v} \frac{k \mathrm{K}_1(\beta_{i,mn})}{k_{z,mn,o} W(k_{z,mn})} \frac{\iint_{S_o} \cos\left(\frac{m\pi x}{b_i + l\tan\theta}\right) \cos\left(\frac{n\pi y}{h}\right) \mathrm{d}x\mathrm{d}y}{\iint_{S_o} \cos^2\left(\frac{m\pi x}{b_i + l\tan\theta}\right) \cos^2\left(\frac{n\pi y}{h}\right) \mathrm{d}x\mathrm{d}y} \tag{A23}$$

$$C_{-,mn} = \frac{C_{+,mn} \mathrm{K}_1(-\beta_{i,mn})}{\mathrm{K}_1(\beta_{i,mn})}. \tag{A24}$$

Substituting Equations (A23) and (A24) into Equation (11), the 3D solution of the pressure is obtained as follows:

$$p(x, y, z) = \rho_0 c \overline{v} \sum_{m=0}^{\infty} \sum_{n=0}^{\infty} \frac{U(k_{z,mn}, z)}{W(k_{z,mn})} \frac{k}{k_{z,mn,o}} \frac{\cos\left(\frac{m\pi x}{b_i + z\tan\theta}\right) \cos\left(\frac{n\pi y}{h}\right) \iint_{S_o} \cos\left(\frac{m\pi x}{b_i + l\tan\theta}\right) \cos\left(\frac{n\pi y}{h}\right) \mathrm{d}x\mathrm{d}y}{\iint_{S_o} \cos^2\left(\frac{m\pi x}{b_i + l\tan\theta}\right) \cos^2\left(\frac{n\pi y}{h}\right) \mathrm{d}x\mathrm{d}y} \tag{A25}$$

where

$$U(k_{z,mn}, z) = \mathrm{K}_1(\beta_{i,mn}) \mathrm{K}_0(-\beta_{mn}) + \mathrm{K}_0(\beta_{mn}) \mathrm{K}_1(-\beta_{i,mn}). \tag{A26}$$

Substituting Equation (A25) with $z = 0$ into Equation (16) to obtain the average pressure at the inlet as follows:

$$
\begin{aligned}
p_i &= \frac{1}{S_i}\iint_{S_i}\left\{\rho_0 c\overline{v}\sum_{m=0}^{\infty}\sum_{n=0}^{\infty}\frac{U(k_{z,mn},0)}{W(k_{z,mn})}\frac{k}{k_{z,mn,o}}\frac{\cos\left(\frac{m\pi x}{b_i}\right)\cos\left(\frac{n\pi y}{h}\right)\iint_{S_o}\cos\left(\frac{m\pi x}{b_i+l\tan\theta}\right)\cos\left(\frac{n\pi y}{h}\right)\mathrm{d}x\mathrm{d}y}{\iint_{S_o}\cos^2\left(\frac{m\pi x}{b_i+l\tan\theta}\right)\cos^2\left(\frac{n\pi y}{h}\right)\mathrm{d}x\mathrm{d}y}\right\}\mathrm{d}x\mathrm{d}y \\
&= \rho_0 c\overline{v}\left\{\begin{array}{l}
\underbrace{\frac{U(k,z)}{W(k)}}_{E_{31}} + \underbrace{\sum_{m=1}^{\infty}\frac{U(k_{z,m0,i},0)}{W(k_{z,m0})}\frac{2k}{k_{z,m0,o}}\left(\frac{2}{m\pi}\right)^2\Psi_{lb2}\Psi_{b1}}_{E_{32}} \\
\quad + \underbrace{\sum_{n=1}^{\infty}\frac{U(k_{z,0n,i},0)}{W(k_{z,0n})}\frac{2k}{k_{z,0n,o}}\left(\frac{2}{n\pi}\right)^2\Psi_{h2}\Psi_{h1}}_{E_{33}} \\
\quad + \underbrace{\sum_{m=1}^{\infty}\sum_{n=1}^{\infty}\frac{U(k_{z,mn,i},0)}{W(k_{z,mn})}\frac{4k}{k_{z,mn,o}}\left(\frac{4}{mn\pi^2}\right)^2\Psi_{lb2}\Psi_{h2}\Psi_{b1}\Psi_{h1}}_{E_{34}}
\end{array}\right\} \\
&= \rho_0 c\overline{v}E_3
\end{aligned}
\tag{A27}
$$

where

$$E_3 = E_{31} + E_{32} + E_{33} + E_{34}. \tag{A28}$$

The quantity E_{31} is obtained with $m = 0$ and $n = 0$. E_{32} is obtained with $m \geq 1$ and $n = 0$. E_{33} is obtained with $m = 0$ and $n \geq 1$. Additionally, E_{34} is obtained with $m \geq 1$ and $n \geq 1$.

Substituting Equation (A25) and $z = l$ into Equation (17) to obtain the average pressure at the outlet as follows:

$$
\begin{aligned}
p_o &= \frac{1}{S_o}\iint_{S_o}\left\{\rho_0 c\overline{v}\sum_{m=0}^{\infty}\sum_{n=0}^{\infty}\frac{U(k_{z,mn},l)}{W(k_{z,mn})}\frac{k}{k_{z,mn,o}}\frac{\cos\left(\frac{m\pi x}{b_i+l\tan\theta}\right)\cos\left(\frac{n\pi y}{h}\right)\iint_{S_o}\cos\left(\frac{m\pi x}{b_i+l\tan\theta}\right)\cos\pi\left(\frac{n\pi y}{h}\right)\mathrm{d}x\mathrm{d}y}{\iint_{S_o}\cos^2\left(\frac{m\pi x}{b_i+l\tan\theta}\right)\cos^2\left(\frac{n\pi y}{h}\right)\mathrm{d}x\mathrm{d}y}\right\}\mathrm{d}x\mathrm{d}y \\
&= \rho_0 c\overline{v}\left\{\begin{array}{l}
\underbrace{\frac{U(k,l)}{W(k)}}_{E_{41}} + \underbrace{\sum_{m=1}^{\infty}\frac{U(k_{z,m0,o},l)}{W(k_{z,m0})}\frac{2k}{k_{z,m0,o}}\left(\frac{2}{m\pi}\Psi_{lb2}\right)^2}_{E_{42}} \\
\quad + \underbrace{\sum_{n=1}^{\infty}\frac{U(k_{z,0n,o},l)}{W(k_{z,0n})}\frac{2k}{k_{z,0n,o}}\left(\frac{2}{n\pi}\Psi_{h2}\right)^2}_{E_{43}} \\
\quad + \underbrace{\sum_{m=1}^{\infty}\sum_{n=1}^{\infty}\frac{U(k_{z,mn,o},l)}{W(k_{z,mn})}\frac{4k}{k_{z,mn,o}}\left(\frac{4}{mn\pi^2}\Psi_{lb2}\Psi_{h2}\right)^2}_{E_{44}}
\end{array}\right\} \\
&= \rho_0 c\overline{v}E_4
\end{aligned}
\tag{A29}
$$

where

$$E_4 = E_{41} + E_{42} + E_{43} + E_{44}. \tag{A30}$$

The quantity E_{41} is obtained with $m = 0$ and $n = 0$. E_{42} is obtained with $m \geq 1$ and $n = 0$. E_{43} is obtained with $m = 0$ and $n \geq 1$. Additionally, E_{44} is obtained with $m \geq 1$ and $n \geq 1$. The elements B and D can be calculated from Equations (19), (A18), (A19), (A27) and (A29) with the following equations

$$B = \frac{\rho_0 c\overline{v}E_3 - A\rho_0 c\overline{v}E_4}{v_o} = \frac{\rho_0 c\overline{v}E_3 - A\rho_0 c\overline{v}E_4}{\overline{v}} = \rho_0 c\left(E_3 - \frac{E_1 E_4}{E_2}\right) \tag{A31}$$

$$D = -\frac{C\rho_0 c\overline{v}E_4}{v_0} = -\frac{C\rho_0 c\overline{v}E_4}{\overline{v}} = \frac{E_4}{E_2}. \tag{A32}$$

Appendix B. FEM Methodology

Figure A1 shows the FEM model used the automatic matched layer (AML) method [33] in LMS Virtual.Lab software to calculate TL. Tetrahedral mesh (2 mm) was used to guarantee the calculation accuracy and the total number of grid cells of every REC was more than 400,000. The fluid material among the REC was defined as air, whose velocity was 340 m/s and density was 1.225 kg/m^3. Then, the outlet was AML property, which could simulate the nonreflecting boundary condition. The inlet acoustic boundary condition was defined as the plane wave with 1 W sound power.

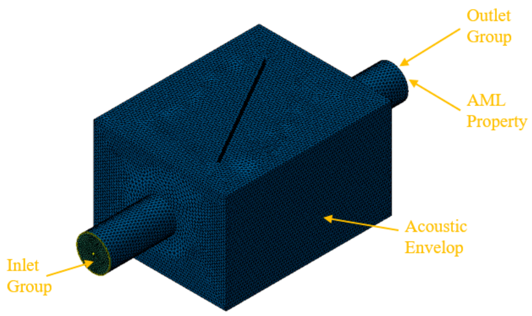

Figure A1. The FEM model of the REC.

References

1. Sun, Y.H.; Zhang, J.; Han, J.; Gao, Y.; Xiao, X.B. Acoustic transmission characteristics and optimum design of the wind ducts of high-speed train. *J. Mech. Eng. Chin. Ed.* **2018**, *54*, 129–137. (In Chinese) [CrossRef]
2. Sun, Y.H.; Zhang, J.; Han, J.; Gao, Y.; Xiao, X.B. Sound transmission characteristics of silencer in wind ducts of high-speed train. *J. Zhejiang Univ. Eng. Sci.* **2019**, *53*, 1389–1397. (In Chinese)
3. Gopalakrishnan, S.; Raut, M.S. Longitudinal wave propagation in one-dimensional waveguides with sinusoidally varying depth. *J. Sound Vib.* **2019**, *463*, 114945. [CrossRef]
4. Assis, G.F.C.A.; Beli, D.; Miranda, E.J.P., Jr.; Camino, J.F.; Dos Santos, J.M.C.; Arruda, J.R.F. Computing the complex wave and dynamic behavior of one-dimensional phononic systems using a state-space formulation. *Int. J. Mech. Sci.* **2019**, *163*, 105088. [CrossRef]
5. Liu, J.; Wang, T.; Chen, M. Analysis of sound absorption characteristics of acoustic ducts with periodic additional multi-local resonant cavities. *Symmetry* **2021**, *13*, 2233. [CrossRef]
6. Terashima, F.J.H.; de Lima, K.F.; Barbieri, N.; Barbieri, R.; Filho, N.L.M.L. A two-dimensional finite element approach to evaluate the sound transmission loss in perforated silencers. *Appl. Acoust.* **2022**, *192*, 108694. [CrossRef]
7. Junge, M.; Brunner, D.; Walz, N.-P.; Gaul, L. Simulative and experimental investigations on pressure-induced structural vibrations of a rear muffler. *J. Acoust. Soc. Am.* **2010**, *128*, 2782–2791. [CrossRef]
8. Liu, L.L.; Zheng, X.; Hao, Z.Y.; Qiu, Y. A computational fluid dynamics approach for full characterization of muffler without and with exhaust flow. *Phys. Fluids* **2020**, *32*, 066101.
9. Liu, L.L.; Hao, Z.Y.; Zheng, X.; Qiu, Y. A hybrid time-frequency domain method to predict insertion loss of intake system. *J. Acoust. Soc. Am.* **2020**, *148*, 2945. [CrossRef]
10. Liu, L.L.; Zheng, X.; Hao, Z.Y.; Qiu, Y. A time-domain simulation method to predict insertion loss of a dissipative muffler with exhaust flow. *Phys. Fluids* **2021**, *33*, 067114. [CrossRef]
11. Tolstoy, I. The WKB approximation, turning points, and the measurement of phase velocities. *J. Acoust. Soc. Am.* **1972**, *52*, 356–363. [CrossRef]
12. Subrahmanyam, P.B.; Sujith, R.I.; Lieuwen, T.C. A family of exact transient solutions for acoustic wave propagation in inhomogeneous, non-uniform area ducts. *J. Sound. Vib.* **2001**, *240*, 705–715. [CrossRef]
13. Li, J.; Morgans, A.S. The one-dimensional acoustic field in a duct with arbitrary mean axial temperature gradient and mean flow. *J. Sound. Vib.* **2017**, *400*, 248–269. [CrossRef]
14. Rani, V.K.; Rani, S.L. WKB solutions to the quasi 1-D acoustic wave equation in ducts with non-uniform cross-section and inhomogeneous mean flow properties—Acoustic field and combustion instability. *J. Sound. Vib.* **2018**, *436*, 183–219. [CrossRef]
15. Basu, S.; Rani, S.L. Generalized acoustic Helmholtz equation and its boundary conditions in a quasi 1-D duct with arbitrary mean properties and mean flow. *J. Sound. Vib.* **2021**, *512*, 116377. [CrossRef]
16. Eisner, E. Complete solutions of the "Webster" horn equation. *J. Acoust. Soc. Am.* **1967**, *41*, 1126–1146. [CrossRef]
17. Miles, J.H. Verification of a one-dimensional analysis of sound propagation in a variable area duct without flow. *J. Acoust. Soc. Am.* **1982**, *72*, 621–624. [CrossRef]
18. Lee, S.K.; Mace, B.R.; Brennan, M.J. Wave propagation, reflection and transmission in non-uniform one-dimensional waveguides. *J. Sound. Vib.* **2007**, *304*, 31–49. [CrossRef]
19. Martin, P.A. On Webster's horn equation and some generalizations. *J. Acoust. Soc. Am.* **2014**, *116*, 1381–1388. [CrossRef]
20. Donskoy, D.M. Directionality and gain of small acoustic velocity horns. *J. Acoust. Soc. Am.* **2017**, *142*, 3450–3458. [CrossRef]

21. Pagneux, V.; Amir, N.; Kergomard, J. A study of wave propagation in varying cross-section waveguides by modal decomposition. Part I. Theory and validation. *J. Acoust. Soc. Am.* **1996**, *100*, 2034–2048. [CrossRef]
22. Amir, N.; Pagneux, V.; Kergomard, J. A study of wave propagation in varying cross-section waveguides by modal decomposition. Part II. Results. *J. Acoust. Soc. Am.* **1997**, *101*, 2504–2517. [CrossRef]
23. Maurel, A.; Mercier, J.F.; Pagneux, V. Improved multimodal admittance method in varying cross section waveguides. *Proc. Math. Phys. Eng. Sci.* **2014**, *470*, 20130448. [CrossRef] [PubMed]
24. Pillai, M.A.; Ebenezer, D.D.; Deenadayalan, E. Transfer matrix analysis of a duct with gradually varying arbitrary cross-sectional area. *J. Acoust. Soc. Am.* **2019**, *146*, 4435–4445. [CrossRef] [PubMed]
25. Munjal, M.L. *Acoustics of Ducts and Mufflers*, 2nd ed.; John Wiley & Sons: New York, NY, USA, 2014.
26. Polyanin, A.D.; Zaitsev, V.F. *Handbook of Exact Solutions for Ordinary Differential Equations*; CRC Press: Boca Raton, FL, USA, 1995.
27. Fucci, G.; Kirsten, K. Expansion of infinite series containing modified Bessel functions of the second kind. *J. Phys. A Math. Theor.* **2015**, *48*, 435203. [CrossRef]
28. Torregrosa, A.J.; Broatch, A.; Payri, R. A study of the influence of mean flow on the acoustic performance of Herschel–Quincke tubes. *J. Acoust. Soc. Am.* **2000**, *107*, 1874–1879. [CrossRef]
29. Ih, J.G. The reactive attenuation of rectangular plenum chambers. *J. Sound. Vib.* **1992**, *157*, 93–122. [CrossRef]
30. Mechel, F.P. *Formulas of Acoustics*, 2nd ed.; Springer: Berlin/Heidelberg, Germany, 2008.
31. *ASTM E2611-09*; Standard Test Method for Measurement of Normal Incidence Sound Transmission of Acoustical Materials Based on the Transfer Matrix Method. ASTM International: West Conshohocken, PA, USA, 2009.
32. ANSYS Inc. *Ansys Fluent 19.1 Theory Guide*; ANSYS Inc.: Canonsburg, PA, USA, 2018.
33. Fu, J.; Chen, W.; Tang, Y.; Yuan, W.H.; Li, G.M.; Li, Y. Modification of exhaust muffler of a diesel engine based on finite element method acoustic analysis. *Adv. Mech. Eng.* **2015**, *7*, 1–2. [CrossRef]